Sensitivity of mid-ocean ridge hydrothermal system controlled by the detachment fault to the glacial cycle

Xianhui Yang
  Shanghai Jiao Tong University

Chunhui Tao (✉ taochunhuimail@163.com)
  Second Institute of Oceanography, MNR   https://orcid.org/0000-0003-3186-1447

Shili liao
  Second Institute of Oceanography, Ministry of Natural Resources

Fernando Barriga

Xianming Deng
  Key Laboratory of Submarine Geosciences, Second Institute of Oceanography, Ministry of Natural Resources

Jin Liang
  Key Laboratory of Submarine Geosciences, Second Institute of Oceanography, Ministry of Natural Resources

Zhikui Guo
  GEOMAR Helmholtz Centre for Ocean Research Kiel

Mingxu Wang
  Shanghai Jiao Tong University

Weifang Yang
  Key Laboratory of Submarine Geosciences, Second Institute of Oceanography, Ministry of Natural Resources

---

Abstract

Changes in sea level caused by glacial cycles may influence the magmatism and hydrothermal activity of oceanic ridges. Recent studies showed that the response time of the hydrothermal activity in the intermediate-fast spreading ridges differs from that in the slow-spreading ridges to the glacial cycles, and a unified model is expected to explain it. Here, we report the 160 ka sediment record adjacent to the Yuhuang hydrothermal field on the Southwest Indian Ridge. Hydrothermal and detachment fault activities were found to enhance or weaken during glacial and interglacial periods, respectively. The magmatism of slow/ultraslow spreading ridges is more sensitive to sea level changes; with the synchronous effect of detachment faults, the hydrothermal activity responds faster to the glacial cycles. We established a model of Sea level change−Magmatism−Detachment fault activity−Hydrothermal activity to explain the different responses of the hydrothermal activity of the mid-ocean ridges to the glacial cycles.

Introduction

Hydrothermal activity in mid-ocean ridges facilitates the chemical exchange of seawater with the new oceanic crust[1]. Modified seawater is rich in gases such as CO_2, CH_4, H_2, H_2S and metallic elements such as Fe, Mn, Cu, and Zn, discharged from the seafloor to provide the ocean with a material flux comparable to that of river inputs, potentially affecting biogeochemical cycles on a global scale while forming large-scale seafloor polymetallic sulfide deposits[1−3].

Recent studies showed that in the fast-spreading East Pacific Rise (EPR 1°N, 6°S, 11°S, and 19°S)[4,5] and the intermediate spreading Juan de Fuca Ridge (JDFR 45°N)[6], when the glaciers began to melt during the glacial terminations, hydrothermal activity increased, most of which increased by approximately 0.5−1.5 times, suggesting that it may be related to the rapid decline in sea level during the glacial period[4,5,6]. Similar phenomena were also observed in the Trans-Atlantic Geotraverse (TAG) hydrothermal field on the slow-spreading North Mid-Atlantic Ridge (NMAR); however, the hydrothermal enhancement events occurred in the active period of glaciers adjacent to the events of rapid sea level decline[7,8]. This enhancement event of hydrothermal activity associated with the glacial cycle has been explained as follows: the rapid decline in sea level in the glacial period reduced the pressure on the mantle beneath the oceanic ridge, and thus increased the melt production, leading to the enhancement of hydrothermal activity due to a more robust heat source supply[9]. However, the hydrothermal activity of the slow-spreading ridge is inconsistent with the response time of the intermediate-fast spreading ridge to the glacial cycle. The response of the slow ridge to sea level decline is faster, while the response of the intermediate-fast ridge is delayed for nearly the entire glacial period. This difference in the timeline has not been properly explained.

The hydrothermal activity mostly occurs on the detachment fault of the asymmetric accretion segment on the slow-ultraslow spreading ridge, which is characterized by limited magma supply at depth and exposed lower crust and mantle materials on the seafloor[10−12]. Deep faults can readily extract heat from

deeper heat sources. Moreover, the repeated movement of faults activates the permeable fluid channels of the overlying oceanic crust, thus driving the long-life hydrothermal cycle[13–15]. The mechanism of heat mining of a fault-controlled hydrothermal system is very different from the magma-dominated companion commonly seen in the intermediate-fast spreading ridge (such as EPR and JDFR). This holds regardless of the heat source, hydrothermal circulation depth and fluid composition, hydrothermal activity life, stability over time, etc.[13,14,16,17]. Therefore, the response of hydrothermal activity to the glacial cycle would also be different between hydrothermal systems with different types and spreading rates of the host ridge segments.

The study area is located in the Yuhuang hydrothermal field (HF) on the Southwest Indian Ridge (SWIR) (Fig. 1a). The full spreading rate of the SWIR is between 1.4–1.6 cm/a, typical for an ultra-slow-spreading ridge[18]. Widespread hydrothermal activity occurs along the SWIR, with much more frequent hydrothermal activity occurring than originally estimated[2,12]. The inactive Yuhuang HF is located on a linear uplift crustal piece approximately 8 km south of the neovolcanic ridge[12,19](Fig. 1b). Recent studies have revealed that the Yuhuang HF is located on the hanging wall of a detachment fault, and thus controlled by tectonic activity and affected by magmatic activity, and its sulfide formation is multi-stage[17,20]. The presence of a large detachment fault in this area, as well as hot anomalous magma, maintains long-term hydrothermal activity in the Yuhuang HF, forming a large (and rare) accumulation of 45.1 Mt of seafloor massive sulfides[11,17,19].

Based on two sediment cores collected near the Yuhuang HF in this study(Fig. 1b), we obtained high-resolution sediment history records covering three glacial periods, which provide a unique opportunity to understand the 160 ka history of hydrothermal, volcanic, and tectonic activity on the ultraslow spreading ridge, and also to elucidate the response mechanism of detachment-controlled hydrothermal activity in relation to the glacial cycle. We found that the hydrothermal activity of Yuhuang HF increased significantly during the glacial period, and more active detachment fault activity appeared at the same time. After the end of the glacial period, both activities are reduced simultaneously. We conclude that in the slow-ultraslow spreading ridge, the magmatism regulated by sea level changes may control the evolution of detachment faults and hydrothermal circulations.

Results

Sediment composition and geochemistry. Mid-ocean ridge sediments are generally comprised of detritus, pelagic biomass materials (calcareous and siliceous), and hydrothermal components[21,22]. Among them, the detritus composition is sourced from local rock weathering materials (basalt and ultramafic rock)[21,22]. From optical microscopy study and chemical analyses, we classify the sediments in the study area as mainly calcareous biological ($CaCO_3$: layer average = 80.00–84.60%), followed by fragmental layers. The average contents of diagenetic elements SiO_2, Al_2O_3, TFe_2O_3, MgO, and TiO_2 are higher than those of the background sediments (Table S1), representing the input of clastic rock in the study area. The layers where the contents of Cr, and Ni are significantly higher than those of the background

sediments may indicate the input of ultramafic clasts[22,23]. This interpretation is supported by the fact that some ultramafic rocks have been collected in the study area[19,22,24]. The contents of Cu, Zn, Fe, Mn, and As are significantly higher than those of the background sediments (Table S2), which may reflect the influence of hydrothermal source materials in these sediments[22,23].

In the Fe−Al−Mg diagram (Fig. S1a), the composition of the sediment in the study area is mostly close to the background sediment and basalt, indicating that the clastic material is mainly basaltic. Some samples deviate from the basaltic field and are closer to the ultramafic rock field, showing the input of ultramafic rock composition. In the Si−Fe−10Mn diagram (Fig. S1b), most of the sediment samples in the study area fall between the background sediment, basalt, and ultramafic rock. This is similar to the sediments from the adjacent Dragon horn area and from the Rainbow and Saldanha HFs controlled by tectonic activity[22,25-27]. Compared with basalt and ultramafic rock, the sediments in the study area have a higher Mn content, which may indicate the input of additional hydrothermal sources (Mn, Fe), hydroxyl oxides, and Mn oxides(Fig. S1b). The sediments in the study area are significantly enriched in Cu and Zn when compared to the background sediment, basalt, and ultramafic rock(Fig. S1c and d), indicating that they are affected by the input of hydrothermal materials. Therefore, the sediments in the study area can be interpreted as a mixture of background sediments, basalt and ultramafic rock fragments, and hydrothermal materials.

History of hydrothermal accumulation. In the study of sedimentary history, element flux is a better indicator of historical changes in material input than elemental content[23,28]. The calculation of the hydrothermal components of sediments, and their fluxes, are described in the subsection of the Methods section. Figure 2 shows the calculated fluxes of hydrothermal-associated Fe, Mn, Cu, and Zn elements derived from the two sediment cores. The hydrothermal deposition fluxes from both sediment cores appear to vary in stages. In core 65gc01, a significant increase in hydrothermal Fe flux occurs at 3−5, 13−15, and 17−21 ka BP(Fig. 2c), whereas significant decreases in hydrothermal Cu and Zn fluxes occur at 10−14 ka BP(Fig. 2d). In core 65gc02, significant increases in hydrothermal Fe flux occur at 10−20, 43−54, 128−139 and >145 ka BP(Fig. 2C), whereas significant increases in hydrothermal Cu and Zn fluxes occur at 10−40, 56−82 and >129 ka BP(Fig. 2D). The hydrothermal fluxes of the sediment cores decrease exponentially with increasing distance from the HF. Both sediment cores show an increase in the hydrothermal deposition during the last glacial period (~ 20 ka BP), reflecting that they may have been influenced by the same event. Closer to the hydrothermal field, core 65gc01 records three episodes of increased hydrothermal activity which lasted 23 ka. Farther from the hydrothermal field, core 65gc02 shows a history of 160 ka of hydrothermal activity, with three large events of hydrothermal activity enhancement, corresponding to three periods of climatic cooling below – 80 m relative to sea level (Marine Isotope Stages (MIS) 2, 4, 6) (Fig. 2B). Hydrothermal Cu element is more sensitive to vent fluid temperature than Fe elements, and hydrothermal Cu/Fe can act as an indicator of vent fluid temperature[6]. In core 65gc02, the hydrothermal vent fluid temperature increased simultaneously during 3 hydrothermal enhancement periods (Fig. 2E).

History of volcanic and tectonic activity. The contents of Al and Ti are relatively stable in oceanic basalts (Al: average = 8.0 wt%; Ti: average = 0.8 wt%), much lower in ultramafic rocks (Al: average = 0.7 wt%; Ti: average = 0.01 wt%) and even more scarce in pelagic calcareous sediments (Table S1, S3). Therefore, Al_2O_3 and TiO_2 can be used as proxies for basalt detrital components in mid-ocean ridge sediments[8,22,23]. Cr and Ni elements are abnormally enriched in ultramafic rocks (Cr: average = 2500 ppm; Ni: average = 1800 ppm) and much lower in basalt (Cr: average = 300 ppm; Ni: average = 140 ppm), and even less in pelagic calcareous sediments[22] (Table S2, S3). Cr/Al and Ni/Al can be used as proxy indicators of ultramafic rock debris input in sediments[23]. The input of basaltic debris to the sediments may have two sources: basaltic eruptions during mid-ocean ridge magmatism or the fragmentation and transport of seafloor basalt during tectonic activity. In contrast, the ultramafic detrital component is derived only from the tectonic activity associated with detachment faults. In core 65gc02, the basalt detrital component had a fluctuation period of approximately 20 ka and the ultramafic component had a similar fluctuation period (Figs. 2F, G). In particular, the simultaneous enhancement of basaltic and ultramafic debris input during the three glacial ages (MIS 2, 4, 6) may indicate an intensification of tectonic activity associated with detachment faults during the same period. In contrast, the enhanced basaltic debris input at 88 and 105 ka BPmight have been derived from enhanced mid-ocean ridge magmatism. Additionally, the two glacial termination periods (140 and 14 ka BP) show significantly stronger basaltic debris input than other historical periods and significantly weaker ultramafic debris input during the same period, which may indicate a significant intensification of mid-ocean ridge magmatism and suppression of detachment fault activity during this period. A similar phenomenon also occurs during MIS 3. Enhanced magmatism during the glacial termination is found on the East Pacific Rise, Juan de Fuca Ridge, Central Indian Ridge, and North Atlantic Ridge[4,6,8,29]. In core 65gc01, the performance during the last glacial period (MIS2) is similar to that of core 65gc02 (Fig. 2f, g).

Discussion

Origin of hydrothermal material. The hydrothermal source material of the sediment cores may have been deposited by diffusion from the hydrothermal plume or weathering of the sulfide mounds by bottom currents or gravity. The two sediment cores are 8–14 km away from the known Yuhuang HF and are more likely to be derived from the diffusive deposition by the Yuhuang hydrothermal plume rather than from the direct transport of HF sulfide mounds (Fig. 1b). Optical observations, geochemical analyses, and planktonic foraminiferal $\delta^{18}O$ data also do not reflect a clear tectonic event (Tables S1, S2, Figs. S3, S4). Moreover, it is unlikely that weathered transported hydrothermal material would reproduce similar vertical changes of hydrothermal elements on sediment cores in multiple directions (Fig. 2). We conclude that the vertical changes in hydrothermal elements of the two sediment cores are mainly influenced by the diffuse deposition of hydrothermal plumes during the active historical period in the Yuhuang HF, which can reflect the intensity of hydrothermal material expelled from the Yuhuang HF vents.

Effect of the glacial cycle in hydrothermal activity in different oceanic ridges. The response of hydrothermal activity to the glacial-interglacial cycle has been discovered in the sediment records of four

sections of the ridges (JdFR, EPR, MAR, and SWIR, this study) in the middle and low latitudes (37°S–45°N) of the Atlantic, Pacific, and Indian oceans (Figs. 3, 4). The consistent understanding of the trigger mechanism for the increase in hydrothermal flux at glacial termination is that the significant decline in sea level during the glacial period reduces the pressure on the seafloor, which promotes an increase in upper mantle melting. The augmented heat supply may increase the intensity of the mid-ocean ridge hydrothermal circulation[4,6,8]. This understanding has also been confirmed by numerical simulation results[9,30]. However, the enhancement of hydrothermal activity recorded by the intermediate-fast spreading ridge did not occur in the period of lowest relative sea level but somewhat later, in the period of rapid sea level rise (Fig. 3, 4). This time shift was interpreted as a result of a restricted melt migration rate, resulting in its failure to provide timely feedback on sea level changes[4,6,9,30]. Alternatively, the hydrothermal activity enhancement recorded by the slow-ultraslow spreading ridge occurred during the entire glacial period and the sea level was at a low level after a rapid decline (Figs. 3, 4).

Sea level change–Magmatism–Detachment fault activity–Hydrothermal activity response Model. Given the difference in the response in the hydrothermal activities to the glacial cycle on the oceanic ridges with different spreading rates, a possible explanation is that the hydrothermal activities of slow-ultraslow spreading ridges are more sensitive to the drop in sea level. This is confirmed by the results of mathematical simulation[9,31], which indicated that the sea level decreased by 60 m within 15 ka, and the increase in magma generation caused by the sea level decrease has the largest impact on the ultraslow spreading ridges (with an increase of 24.6%), followed by slow-spreading ridges (16%), which is 2.0–2.9 and 1.3–1.8 times of the intermediate-fast spreading ridge respectively[31].

By reconstructing the hydrothermal activity history and the region's magmatic and tectonic activity history of the Yuhuang HF on the SWIR, we found that the hydrothermal and detachment fault activities are simultaneous. These activities increased synchronously during the glacial period and decreased synchronously during the deglaciation period (Figs. 2, 4, S6). Therefore, we propose a new mechanism to explain the sea level changes related to the glacial cycle, which regulates the melt supply of the mantle beneath the new volcanic ridge and then regulates the hydrothermal circulation above the detachment fault. The correlation between hydrothermal activity and tectonic activity related to detachment faults has been found at several oceanic ridges[14,15,23,28]. The activity of the detachment fault increases the permeability of the rock and controls the heat injection under the fault, and the repeated movement on the fault activates and controls the hydrothermal circulation on which it occurs[14,15]. Additionally, it has been found that the hydrothermal venting of the large hydrothermal circulation systems on slow-ultraslow spreading ridges may be episodic[7,32,33]. The formation of its multi-hydrothermal mounds may be caused by several short-term hydrothermal eruptions, accounting for 20–50% of the lifespan of the hydrothermal system, with each single eruption lasting about 5–15 ka[7,32,33]. The results of numerical simulation show that the formation of hydrothermal mounds in the TAG HF of the NMAR can activate and drive the hydrothermal circulation on the footwall of a highly permeable detachment fault through periodic magma intrusion[34].

Therefore, we established a unified Sea level change−Magmatism−Detachment fault activity− Hydrothermal activity response Model (Fig. 5). In the intermediate-fast spreading ridge, hydrothermal activity is mainly controlled by magmatism. Due to the rapid spreading rate, the contribution of sea level drop during the glacial period to the increase of melt production under the ocean ridge is relatively minor. Coupled with the limited melt migration rate[9,30], the enhancement of hydrothermal activity was delayed to the glacial termination after the sea level dropped for approximately 10−20 ka (Fig. 5a). During the interglacial period, the rapid sea level rise inhibited the occurrence of magmatism and decreased hydrothermal activity (Fig. 5a). In the asymmetric spreading section of the slow-ultraslow spreading ridges, hydrothermal activity is mainly controlled by detachment faults and influenced by magmatism. Due to the slow spreading rate, melt production under the ocean ridge is more sensitive to the response of the sea level drop during the glacial period. Frequent magma intrusions triggered the hydrothermal circulation above the detachment fault, and the active detachment fault at the same time accelerated the hydrothermal activity during the glacial period (Fig. 5b). In the interglaciation period, the rapidly rising sea level will inhibit melt production, the detachment fault is not active simultaneously and the hydrothermal activity is significantly reduced.

Large variations in mid-ocean ridge hydrothermal flux during the glacial cycles are consistent regardless of the spreading rate, and the control factors behind it may be more complex than previously expected. The slow-ultraslow spreading ridge, particularly, has a longer length (62% of the mid-ocean ridge), a larger hydrothermal mineralization scale (86% of the mid-ocean ridge)[3], and a longer hydrothermal system life (~ 100 ka) than the intermediate-fast spreading ridge. The increased hydrothermal discharge during the glacial period may significantly impact the marine biogeochemical cycle and global climate change, which is noteworthy.

Methods

Sampling. The sediment cores were collected during the Indian Ocean Survey Voyage (DY135-58,65) organized by the Chinese Oceanic Association (COMRA) in 2020 and 2021. The sampling locations were located within the western rift of the Yuhuang HF of the SWIR, 3.4, 7.9, and 13.7 km from the HF, are named 58gc01, 65gc01 and 65gc02 respectively (Fig. 1). Sampling water depths ranging from 3400− 3600 m, above the calcite compensation depth. The sediments were mainly greyish-white−greyish-brown calcareous ooze mud with coring lengths of 40, 65, and 125 cm. Previous deep towing and mooring surveys revealed that bottom currents in this area flow mainly to the northwest, with a maximum velocity of 20−30 cm/s[35]. The bottom flow direction near the Yuhuang HF is roughly north to northwest based on the ripple direction in the seafloor camera photos. The sediment cores are located in the main diffusion direction of the Yuhuang hydrothermal plume.

Geochemical analyses. Geochemical analysis of the sediment cores was conducted at the ALS Laboratory Group in Guangzhou, China. Sediment cores were sectioned at 2 cm intervals, freeze-dried, and large rock fragments were removed and ground to 74 μm (200 mesh) in an agate mortar. The major elements were analyzed using an X-ray fluorescence spectrometer (PANalytical PW2424). Before

analysis, each sample was fully mixed with a flux containing lithium nitrate and heated at 1000°C for about 1 h. After melting, each sample was transferred to a platinum mould to form a flat glass sheet. Three standard samples (GBW07105, NCSDC47009, and SARM-4) were used to monitor the accuracy of data during the analysis. The measurement error of the collected data was within 5%. Trace elements were analyzed in an Agilent 7700x ICP-MS. Approximately 250 mg of each sample was weighed and digested with $HClO_4$, HNO_3, and HF. The solution was evaporated until dry, the residue was drained and dissolved with dilute HCl, and the dissolved samples were analyzed. In the spectra, the results were adjusted for inter-element interference. Reference samples GBM908-10 and MRGeo08 were used as internal standards for data quality control, where the data were measured within a 10% error.

Carbon and oxygen stable isotope tests were conducted at the Key Laboratory of Submarine Geosciences (KLSG), Ministry of Natural Resources (MNR), Hangzhou, China, using the online phosphoric acid method, a Finnigan Delta Plus AD spectrometer fitted with Gas Bench II. After ultrasonic cleaning in deionized water, dominant planktonic foraminiferal species (*Globorotalia Inflata*, 150–250 μm size) were selected for carbon and oxygen stable isotope analysis, with test layers selected at 4 cm intervals. CO_2 extraction for $δ^{13}C$ and $δ^{18}O$ measurements were conducted with pure H_3PO_4 at 72°C for 1 h. Data were calibrated against the NBS-19, GBW04406, and GBW04405 standards. Replicate analysis of the laboratory standards shows a standard deviation better than 0.07‰ for $δ^{13}C$ and $δ^{18}O$. All data are reported relative to the Vienna Peedee Belemnite (VPDB) standard.

Age model. The age model for core 65gc02 was based on stable oxygen isotopes from selected planktonic foraminifera (*Globorotalia Inflata*, 150–250 μm size), which were compared to the standard curve of deep-sea oxygen isotopes recognized by the International Commission on Stratigraphy (LR04) to model the age-depth relationship (Figs. S3, S4, S5).

Since core 65gc01 did not undergo ^{14}C dating, its age model mainly refers to the dating results of the adjacent core 58gc01 (4 km away, Fig. S2). Accelerator mass spectrometry radiocarbon measurements were performed at Beta Analytic, USA, on tests of planktonic foraminifera *Globorotalia Inflata* of sediment core (core 58gc01). The ^{14}C age obtained from the test was corrected for calendar age according to the marine 20 standard, where the test error was ± 30–40 BP (relative to 1950 AD). The oxygen isotope contents and trends of core 58gc01 and core 65gc01 are consistent in the 0–30 cm section, indicating that they are in the same stable depositional process. The oxygen isotope content and trends in the 30–40 cm section show large differences, likely owing to the tectonic events that occurred at this stage in core 58gc01. Core 65gc01 has similar oxygen isotope trends to core 34mc05 at a distance of 127 km from the northeast mid-ocean ridge flank(Fig. S2), indicating that the overall sedimentary environment of core 65gc01 is relatively stable. Moreover, concerning the deposition rate of the upper 0–30 cm of 58gc01, the age of the bottom of core 65gc01 is projected to be about 20 ka, which is similar to that of the bottom of core 34mc05 at 17 ka[36]. In summary, the overall deposition rate of core 65gc01 can be compared to the deposition rate of the upper 0–30 cm of core 58gc01, which is 2.74 cm/ka, resulting in the age-depth model of core 65gc01 (Figs. S3, S5).

Hydrothermally derived elements calculation. The sediments near the HF in the Southwest Indian Ocean are mainly composed of debris, pelagic biomass materials, and hydrothermal components[21,27]. Of these, the detrital component comprises locally volcanically weathered material (basaltic and ultramafic).

According to various authors[22,23], it is possible to calculate the contribution of each end-member component of the sediments as follows. The geochemical data collected for the basalt and ultramafic rocks in the study area show that the basalt has significantly higher Al and Ti contents than the ultramafic rocks (Table S3), in which the Ti present is almost entirely derived from the diagenetic fraction[37]. The excess Ti compared to the background sediments(BGS) could represent an input of basaltic debris. Therefore, the elemental content of the basaltic debris component can be calculated using the following equation:

$$Element_{basaltic} = (Element/Ti)_{basalt} \times (Ti_{total} - Ti_{BGS}) \quad (1)$$

The Cr content of the ultramafic rock fragments in the study area ranged from 1600–3000 ppm, the Ni content ranged from 1200–2300 ppm and the basaltic Cr and Ni contents ranged from 180–360 and 70–200 ppm, respectively (Table S3). Due to the variation range of Cr content in ultramafic rocks is much larger than that of Ni, the excess Ni element is more representative of the input from the ultramafic rock compared to the background sediments and basalt. Therefore, the elemental content of the ultramafic debris component can be calculated using the following equation:

$$Element_{ultramafic} = (Element/Ni)_{ultramafic} \times Ni_{ultramafic} \quad (2)$$

$$Ni_{ultramafic} = Ni_{total} - Ni_{basaltic} - Ni_{BGS}. \quad (3)$$

Finally, the elemental content of the hydrothermal source components can be calculated using the following equation:

$$Element_{hydrothermal} = Element_{total} - Element_{basaltic} - Element_{ultramafic} - Element_{BGS}, \quad (4)$$

where Element/Ti values for basalts and Element/Ni for ultramafic rocks can be obtained from data from supplementary materials, while background sediment elemental content is derived from ref.22.

Hydrothermal accumulation fluxes calculation. The cumulative flux of elements of hydrothermal origin ($[Element]_{flux}$) can be calculated by multiplying the total mass accumulation rate by the concentration of a given element ($[Element]$)[23,38]:

$$[Element]_{flux} = [Element] \times Mass_{flux}[\rho] \times [R], \quad (5)$$

$$Mass\ flux = [\rho] \times [R], \quad (6)$$

where ρ is the dry density of the sediment, calculated using the $CaCO_3$ content[39]; R is the sedimentation rate, derived from the age-depth model for sediment cores in the previous section.

Declarations

Data Availability

The statistics of the geochemical data for the sediments used in this study are reported in Table S1, S2, and S3.

Author Contributions

Chunhui Tao led the project and finished the interpretation. Xianhui Yang prepared the original manuscript, analyses and geochemistry interpretation. Shili Liao, Mingxu Wang, and Zhikui Guo participated in the interpretation of the results. Fernando J.A.S. Barriga participated in the interpretation of the results and the examination of the text. Jin Liang and Xianming Deng participated in data collection at Cruises. Weifang Yang participated in sediment dating analysis. All authors participated in the review of this manuscript.

Competing Interests

The authors declare no competing interests.

References

1. Staudigel, H. Chemical Fluxes from Hydrothermal Alteration of the Oceanic Crust, *Treatise on Geochemistry (Second Edition)* (Elsevier, Oxford,2014).
2. German, C. R., Petersen, S. & Hannington, M. D. Hydrothermal exploration of mid-ocean ridges: Where might the largest sulfide deposits be forming? Chem. Geol. **420**, 114–126(2016).
3. Hannington, M., Jamieson, J., Monecke, T., Petersen, S. & Beaulieu, S. The abundance of seafloor massive sulfide deposits. Geology **39**, 1155–1158(2011).
4. Lund, D. C. *et al.* Enhanced East Pacific Rise hydrothermal activity during the last two glacial terminations. Science **351**, 478–482(2016).
5. Lund, D. C. *et al.* Hydrothermal scavenging of 230Th on the Southern East Pacific Rise during the last deglaciation. Earth Planet. Sci. Lett. **510**, 64–72(2019).
6. Costa, K. M. *et al.* Hydrothermal deposition on the Juan de Fuca Ridge over multiple glacial-interglacial cycles. Earth Planet. Sci. Lett. **479**, 120–132(2017).

7. Dutrieux, A. M. *Rise and fall of a hydrothermal system: A tale of metalliferous sediments (TAG hydrothermal field, MAR, 26°N)*, University of Southampton, (2020).

8. Middleton, J. L., Langmuir, C. H., Mukhopadhyay, S., McManus, J. F. & Mitrovica, J. X. Hydrothermal iron flux variability following rapid sea level changes. Geophys. Res. Lett. **43**, 3848–3856(2016).

9. Lund, D. C. & Asimow, P. D. Does sea level influence mid-ocean ridge magmatism on Milankovitch timescales? Geochem. Geophys. Geosyst. **12**(2011).

10. Escartín, J. *et al.* Central role of detachment faults in accretion of slow-spreading oceanic lithosphere. Nature **455**, 790–794(2008).

11. Li, H. *et al.* Enhanced hydrothermal activity on an ultraslow-spreading supersegment with a seismically detected melting anomaly. Mar. Geol. **430**(2020).

12. Tao, C. *et al.* First active hydrothermal vents on an ultraslow-spreading centre: Southwest Indian Ridge. Geology **40**, 47–50(2012).

13. Tao, C. *et al.* Deep high-temperature hydrothermal circulation in a detachment faulting system on the ultra-slow spreading ridge. Nat. Commun. **11**(2020).

14. Tivey, M. A., Schouten, H. & Kleinrock, M. C. A near-bottom magnetic survey of the Mid-Atlantic Ridge axis at 26°N: Implications for the tectonic evolution of the TAG segment. J. Geophys. Res.: Solid Earth **108**(2003).

15. Wu, T. *et al.* An intermittent detachment faulting system with a large sulfide deposit revealed by multi-scale magnetic surveys. Nat. Commun. **12**, 5642(2021).

16. Fouquet, Y., et al., Geodiversity of hydrothermal processes along the Mid-Atlantic Ridge and ultramafic-hosted mineralization: a new type of oceanic Cu-Zn-Co-Au volcanogenic massive sulfide deposit, Diversity of hydrothermal systems on slow spreading ocean ridges. AGU Geophys. Monograph Series **188**, 321–367 (2010).

17. Zhou, F., Dyment, J., Tao, C. & Wu, T. Magmatism at oceanic core complexes on the ultraslow Southwest Indian Ridge: Insights from near-seafloor magnetics. Geology **50**, 726–730(2022).

18. Jie, C. 780 Thousand Years of Upper-Crustal Construction at a Melt-Rich Segment of the Ultraslow Spreading Southwest Indian Ridge 50°28'E. *J. Geophys. Res.***126**(2021).

19. Yu, J. *et al.* Resource estimation of the sulfide-rich deposits of the Yuhuang-1 hydrothermal field on the ultraslow-spreading Southwest Indian Ridge. Ore Geol. Rev. **134**(2021).

20. Liao, S. *et al.* Two episodes of sulfide mineralization at the Yuhuang-1 hydrothermal field on the Southwest Indian Ridge: Insight from Zn isotopes. Chem. Geol. **507**, 54–63(2019).

21. Chen, X. *et al.* Mineralogy and Geochemistry of Deep-Sea Sediments from the Ultraslow-Spreading Southwest Indian Ridge: Implications for Hydrothermal Input and Igneous Host Rock. Minerals **11**(2021).

22. Liao, S. *et al.* Surface sediment geochemistry and hydrothermal activity indicators in the Dragon Horn area on the Southwest Indian Ridge. Mar. Geol. **398**, 22–34(2018).

23. Cave, R. R., German, C. R., Thomson, J. & Nesbitt, R. W. Fluxes to sediments underlying the Rainbow hydrothermal plume at 36 degrees 14 ' N on the Mid-Atlantic Ridge. Geochim. Cosmochim. Acta **66**, 1905–1923(2002).

24. Ling, C. *et al.* Major and trace elements of abyssal peridotites: evidence for melt refertilization beneath the ultraslow-spreading Southwest Indian Ridge (53deg E segment). Int. Geol. Rev. **57**, 1715–1734(2015).

25. Chavagnac, V., German, C. R., Milton, J. A. & Palmer, M. R. Sources of REE in sediment cores from the Rainbow vent site (36 degrees 14 ' N, MAR). Chem. Geol. **216**, 329–352(2005).

26. Dias, A. S. & Barriga, F. Mineralogy and geochemistry of hydrothermal sediments from the serpentinite-hosted Saldanha hydrothermal field (36 degrees 34 ' N; 33 degrees 26 ' W) at MAR. Mar. Geol. **225**, 157–175(2006).

27. Liao, S. *et al.* Surface sediment composition and distribution of hydrothermal derived elements at the Duanqiao-1 hydrothermal field, Southwest Indian Ridge. Mar. Geol. **416**(2019).

28. Kuhn, T., Burger, H., Castradori, D. & Halbach, P. Volcanic and hydrothermal history of ridge segments near the Rodrigues Triple Junction (Central Indian Ocean) deduced from sediment geochemistry. Mar. Geol. **169**, 391–409(2000).

29. Lim, D. *et al.* Enhancement of volcanic eruption in mid-ocean ridge during the last deglaciation: New sedimentary evidence in the middle part of Central Indian Ridge. Mar. Geol. **440**, 106574(2021).

30. Cerpa, N. G., Rees Jones, D. W. & Katz, R. F. Consequences of glacial cycles for magmatism and carbon transport at mid-ocean ridges. Earth Planet. Sci. Lett. **528**, 115845(2019).

31. Burley, J. M. A. & Katz, R. F. Variations in mid-ocean ridge CO2 emissions driven by glacial cycles. Earth Planet. Sci. Lett. **426**, 246–258(2015).

32. Cherkashov, G. *et al.* Sulfide geochronology along the Northern Equatorial Mid-Atlantic Ridge. Ore Geol. Rev. **87**, 147–154(2017).

33. Yang, W. *et al.* 230Th/238U dating of hydrothermal sulfides from Duanqiao hydrothermal field, Southwest Indian Ridge. Mar. Geophys. Res. **38**, 71–83(2017).

34. Rüpke, L. H. *et al.* Detachment-parallel recharge explains high discharge fluxes at the TAG hydrothermal field. (2021).

35. Liao, G. *et al.* Moored observation of abyssal flow and temperature near a hydrothermal vent on the Southwest Indian Ridge. J. Geophys. Res.: Oceans **121**, 836–860(2016).

36. Jie, Z. Foraminiferal Assemblages in the Southwest Indian ocean Sediments and Their Paleoenrivonmental Implications since Late Pleistocene, China University of Geosciences (Beijing) (2017).

37. Murray, R. W., Leinen, M. & Isern, A. R. Biogenic flux of a1 to sediment in the central equatorial pacific-ocean - evidence for increased productivity during glacial periods. Paleoceanography **8**, 651–670(1993).

38. Qiu, Z. *et al.* The temporal variability of hydrothermal activity of Wocan hydrothermal field, Carlsberg Ridge, northwest Indian Ocean. Ore Geol. Rev. **132**(2021).

39. Snoeckx, H. & Rea, D. K. Dry bulk-density and $CaCO_3$ relationships in upper quaternary sediments of the eastern equatorial pacific. Mar. Geol. **120**, 327–333(1994).

40. Grant, K. M. *et al.* Sea-level variability over five glacial cycles. Nat. Commun. **5**, 5076(2014).

41. Railsback, L. B., Gibbard, P. L., Head, M. J., Voarintsoa, N. R. G. & Toucanne, S. An optimized scheme of lettered marine isotope substages for the last 1.0 million years, and the climatostratigraphic nature of isotope stages and substages. Quat. Sci. Rev. **111**, 94–106(2015).

42. Humphris, S. E., Tivey, M. K. & Tivey, M. A. The Trans-Atlantic Geotraverse hydrothermal field: A hydrothermal system on an active detachment fault. Deep Sea Res. Part II **121**, 8–16(2015).
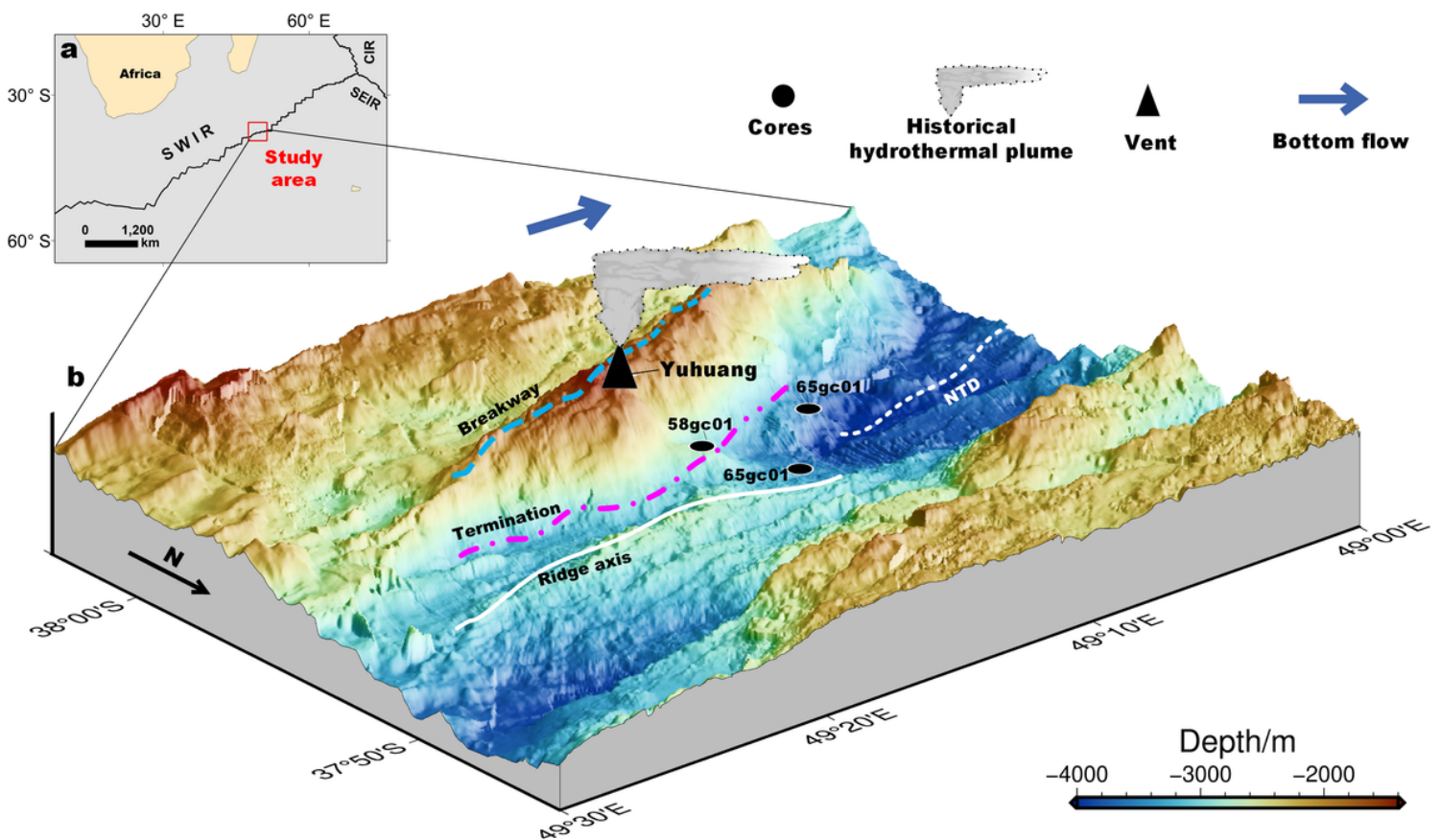
Figures

Figure 1

Map of the study area with the location of marine sediment cores. a Location of the study area; **b** The sampling location of the sediment cores. The cores are named 58gc01, 65gc01 and 65gc02 according to the distance from the hydrothermal field. A high-resolution bathymetry map showing an oblique view from the axial volcanic ridge. The blue thick arrow denotes the bottom flow directions averaged from

seven months of mooring observations[35]. The breakaway and termination lines of the detachment fault at the Yuhuang hydrothermal field are from ref. 17.
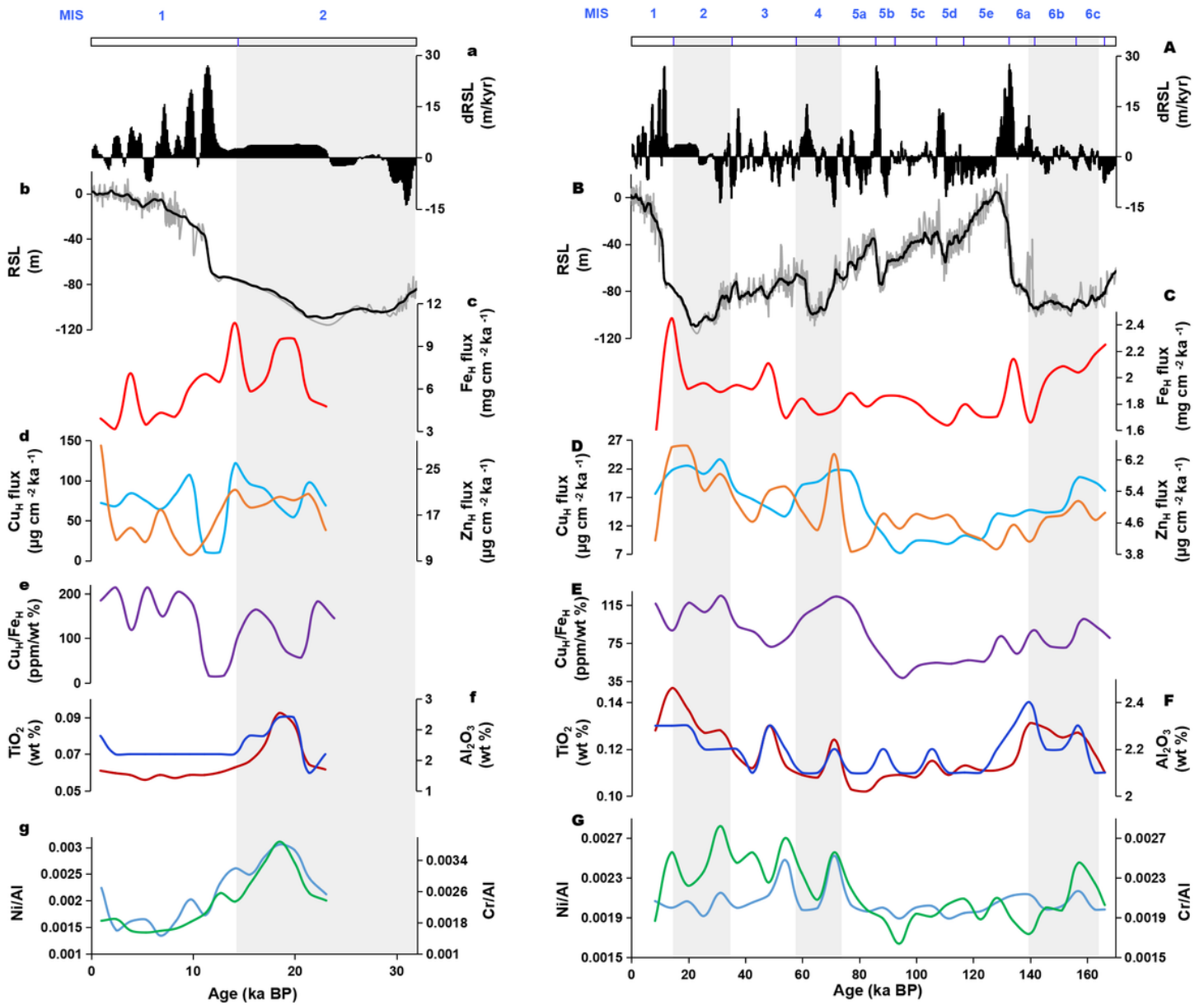

Figure 2

Historical changes of hydrothermal flux in sediment cores. **a (A)** Derivative of relative sea level[40]. **b(B)** Relative sea level[40]. **c(C)** Hydrothermal Fe flux. **d(D)** Hydrothermal Cu flux and Zn flux. **e(E)** Indicator of vent emission temperature: hydrothermal Cu/Fe. **f(F)** Indicator of Basalt debris: Al_2O_3. **g(G)** Indicator of ultramafic rock debris: Ni/Al and Cr/Al. Marine Isotope Stages (MIS) are identified across the top of the figure with blue numbers, in which even stages (also highlighted by grey bars) indicate glacial periods. The data in the left panel (c-g) is derived from core 65gc01, and the data in the right panel(C-G) is derived from core 65gc02.
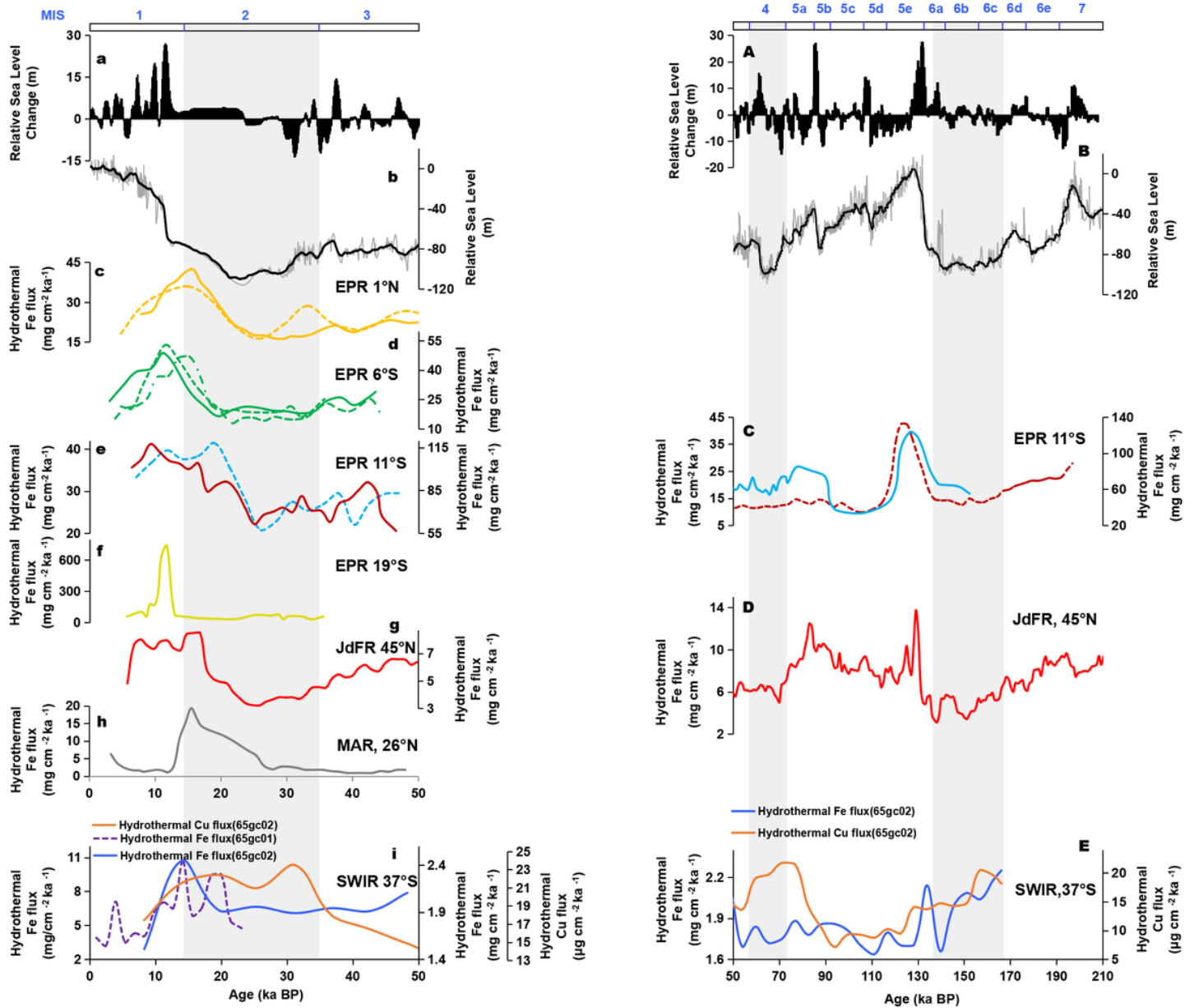
Figure 3

Response of hydrothermal deposition of different ridges to glacial cycle. **a(A)** Derivative of relative sea level[40]. **b(B)** Relative sea level[40]. **c-i, C-E** Hydrothermal Fe flux, and Cu flux, including the JdFR at 45°N[6], the MAR at 26°N[8], the EPR at 1°N, 6°S, 11°S, 19°S[4,5], the SWIR 37°S (this study). Marine Isotope Stages (MIS) are identified across the top of the figure with blue numbers[41], in which even stages (also highlighted by grey bars) indicate glacial periods.
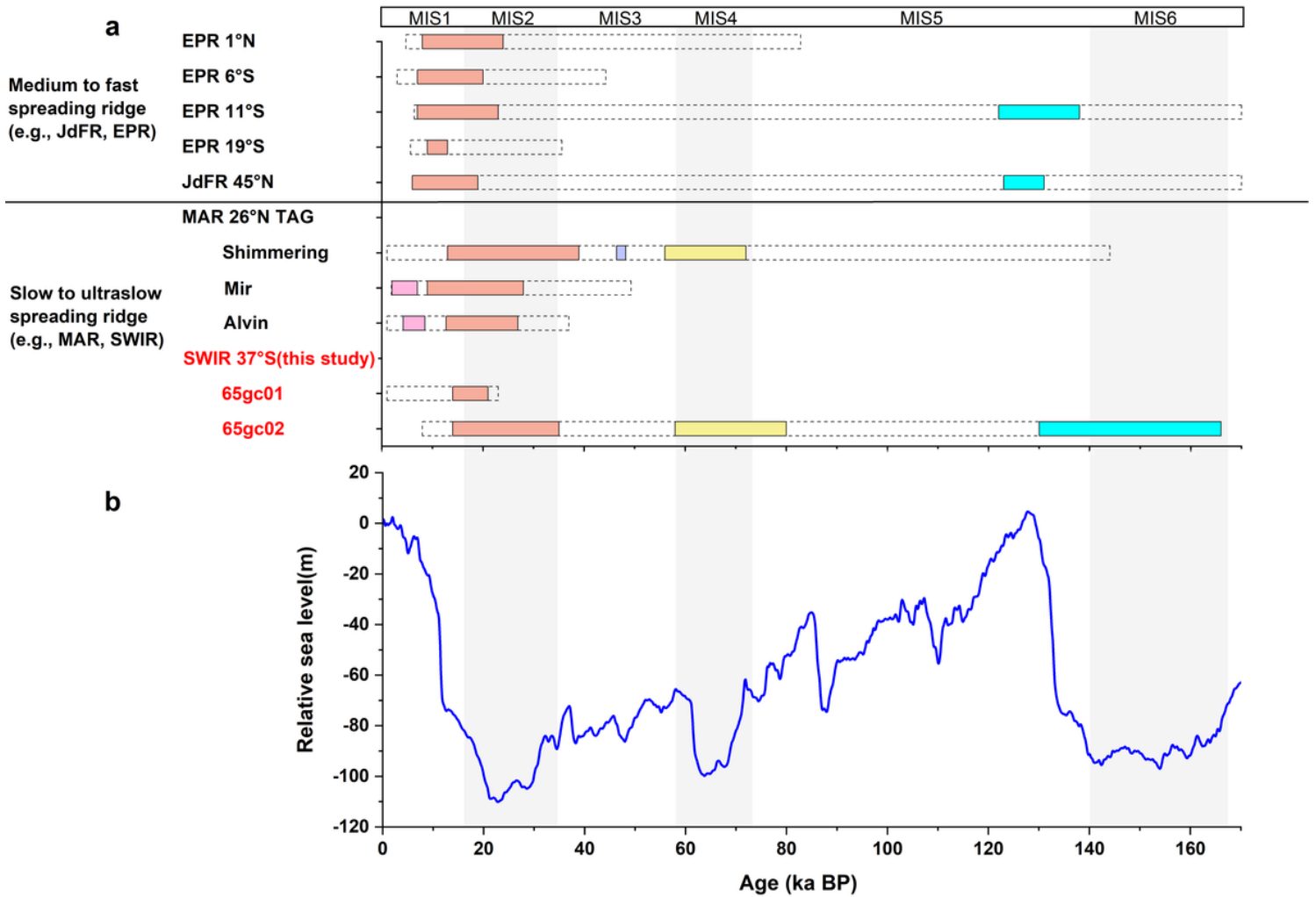
Figure 4

Hydrothermal activity time series of different mid-ocean ridges.

a Hydrothermal activity time series, including the JdFR at 45°N[6], the MAR 26°N, Shimmering and Alvin zone[7], Mir zone[8], the EPR at 1°N, 6°S, 11°S, 19°S[4,5], the SWIR 37°S (this study). b Relative sea level[40]. The dotted boxes represent the entire sedimentary history of the sediment cores, and the coloured boxes represent periods of active hydrothermal activity. Marine Isotope Stages (MIS) are identified across the top of the figure with black numbers[41], in which even stages (also highlighted by grey bars) indicate glacial periods.
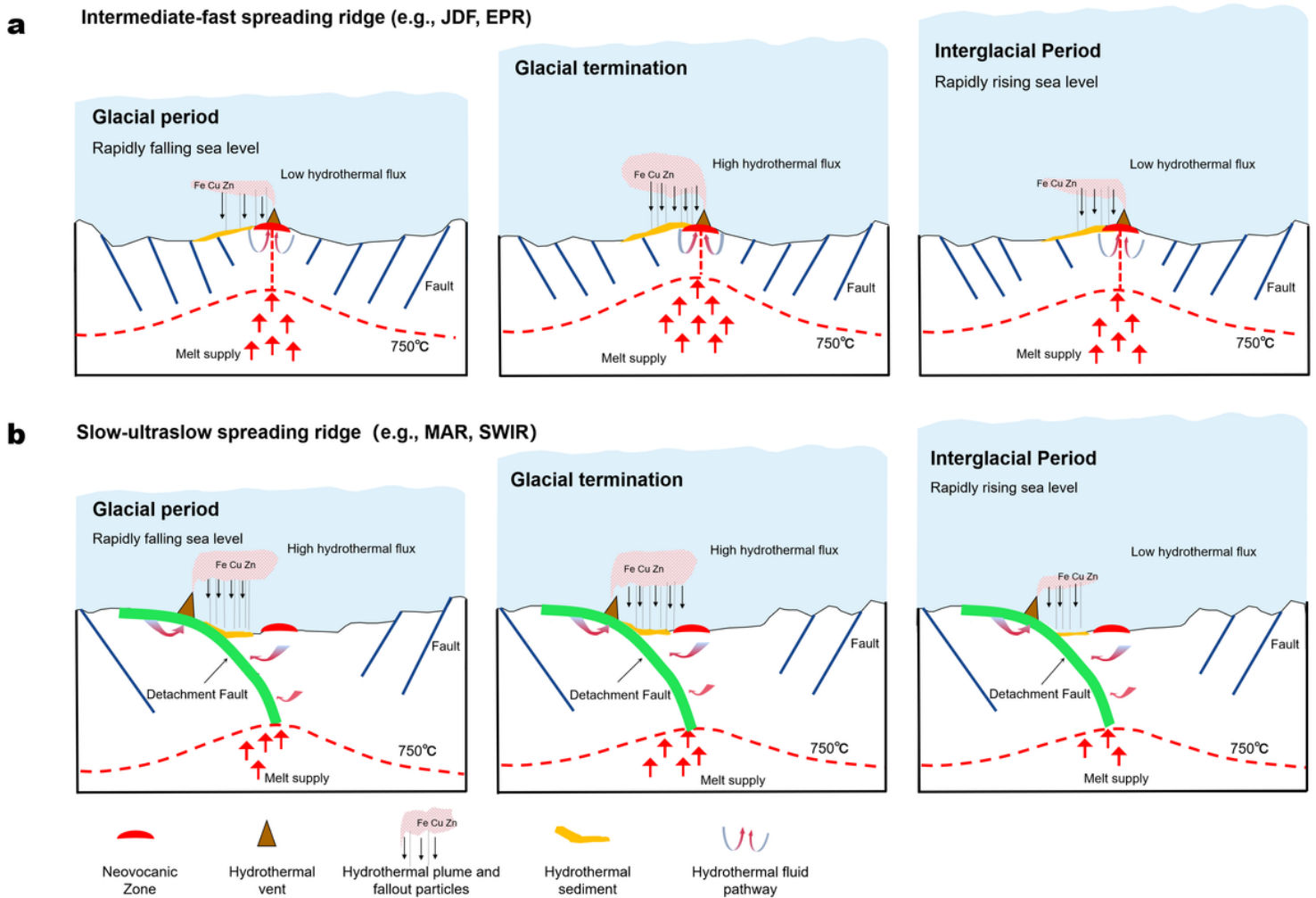
Figure 5

Cartoon of enhanced hydrothermal activity in the glacial cycle. The base map refers to ref. 16 and 42. **a** The model in the intermediate-fast spreading ridge; **b** The model in the slow-ultraslow spreading ridge. It is divided into three periods: glacial period, glacial termination, and interglacial period.

Supplementary Files

This is a list of supplementary files associated with this preprint. Click to download.

- Supplementary.docx